RESEARCH ARTICLE

Contact damage tolerance of alumina-based layered ceramics with tailored microstructures

Josef Schlacher[#] | **Abdullah Jabr**[#] | **Anna-Katharina Hofer** | **Raul Bermejo**

Department of Materials Science, Montanuniversitaet Leoben, Leoben, Austria

Correspondence
Raul Bermejo, Department of Materials Science, Montanuniversitaet Leoben, Franz Josef-Strasse 18, A-8700 Leoben, Austria.
Email: raul.bermejo@unileoben.ac.at

[#]Authors contributed equally to this work.

Abstract

This work demonstrates how to enhance contact damage resistance of alumina-based ceramics combining tailored microstructures in a multilayer architecture. The multilayer system designed with textured alumina layers under compressive residual stresses embedded between alumina–zirconia layers was investigated under Hertzian contact loading and compared to the corresponding monolithic reference materials. Critical forces for crack initiation under spherical contact were detected through an acoustic emission system. Damage was assessed by combining cross-section polishing and ion-slicing techniques. It was found that a textured microstructure can accommodate the damage below the surface by shear-driven, quasi-plastic deformation instead of the classical Hertzian cone cracking observed in equiaxed alumina. In the multilayer system, a combination of both mechanisms, namely Hertzian cone cracking on the top (equiaxed) surface layer and quasi-plastic deformation within the embedded textured layer, was identified. Further propagation of cone cracks at higher loads was hindered and/or deflected owed to the combined action of the textured microstructure and compressive residual stresses. These findings demonstrate the potential of embedding textured layers as a strategy to enhance the contact damage tolerance in alumina ceramics.

KEYWORDS
alumina, Hertzian indentation, multilayers, residual stresses, textured microstructure

1 | INTRODUCTION

Advanced ceramics have been established as materials of choice for many demanding applications. In comparison to metals and polymers, some advantageous properties of ceramics, such as oxidation and corrosion resistance, high temperature stability, high hardness and wear resistance, stiffness, biocompatibility together with interesting functional properties, are the driving factors for the high inter-est in developing ceramic materials.[1,2] However, the inherent brittleness of ceramics (low fracture toughness) along with strength variability are major concerns for safety and reliability issues. Failure of ceramic parts is often associated with the (unstable) propagation of cracks, upon applied mechanical loading, initiated from microstructural defects distributed within or at the surface of components. These flaws may be introduced at the processing step (e.g., pores, agglomerates), during machining of

the parts (surface roughness, scratches) or in-service conditions during the lifetime of the component.[3,4] In this regard, many strategies have been adopted for controlling and reducing the size of critical defects in ceramics, using for instance colloidal processing,[5] or eliminating critical flaws by means of proof testing.[4] However, avoiding failure related to post-processing defects during handling and in service remains a difficult challenge.[6] In this regard, a more prominent strategy has been attempted, which aims to control the propagation of cracks by taking advantage of energy-dissipating toughening mechanisms occurring during the crack propagation events. The so-called "damage tolerant" behavior has been reported in several alumina-based layered ceramic systems designed with embedded (protective) layers under in-plane compressive residual stress.[7–12] In addition, tailoring the microstructure of the protective layers (following the "brick-and-mortar" approach used in bioinspired materials[13]) has significantly enhanced the fracture energy of the system. For instance, texturing the microstructure by aligning platelets parallel to the layer plane has proven to have a positive impact on the mechanical properties of layered ceramic architectures.[14,15] The effect of residual stresses, degree of texture, as well as layer distribution within the multilayer design on the damage tolerance of the ceramic parts has been thoroughly investigated under different loading conditions, such as bending, thermal shock or cycling loading.[16] An important question is how effective such layered design may be against contact loading.

Blunt contact loading, first studied by Hertz,[17] is one of the main sources of failure in advanced ceramics during in-service conditions.[3] In some situations, sudden failure occurs due to the (unstable) propagation of contact cracks, and in some cases failure of ceramic components may also ensue as a consequence of the strength degradation caused by contact-induced damage.[18] In homogeneous, polycrystalline fine-grained ceramics and in glasses, classical Hertzian ring and cone cracking is the typical damage pattern under spherical loading.[19–21] Due to the fact that such macroscopic cracking significantly impairs the strength of ceramic components, much research has been dedicated to restrict deleterious cone crack propagations for increasing their contact damage resistance. One strategy is to introduce "shear-sensitive" microstructural elements within the ceramic material, so that the response of the material to the contact loading scenario leads to subsurface shear faulting rather than cone crack formation starting from the surface.[19] The successful transition from brittle cone cracking to the quasi-plastic damage mode has been reported in ceramics with controlled microstructures, that is, grain coarsening[22,23] or increasing the level of porosity,[24] as well as in hetero-

geneous ceramics containing second phases with weak interface boundaries. Few examples are (i) mica-platelets within a glass matrix,[25] (ii) graphene nanofillers added to silicon carbide,[26] (iii) layered heterogeneous alumina designed with calcium–hexaluminate interfaces,[27,28] or (iv) layered brittle coating systems with enhanced fracture resistance.[29,30]

In this work, we explore the contact damage resistance of novel layered ceramics designed with embedded layers with internal compressive stresses and textured microstructure. The aim of this work is to investigate the effect of texturing on the response of layered alumina ceramics under spherical contact loading scenario. It is hypothesized that the combination of shear-faulting driven micro-failures at the weak basal interfaces of the textured grains with the potential of the in-plane compressive stresses in arresting the propagation of cone cracks may significantly enhance the damage tolerance of the ceramic system. The contact damage behavior is first investigated and compared in monolithic alumina-based samples designed with and without textured microstructures, respectively. Initiation of ring crack is detected by using an acoustic emission (AE) system and confirmed by using polarized light microscopy. Moreover, the underlying damage mechanisms are explored by using cross-sectioning together with the ion-slicing techniques. AE is used for measuring the critical crack initiation forces and the data are analyzed and classified for the different damage mechanisms. The critical crack initiation forces as well as the calculated maximum tensile stresses are analyzed in the framework of Weibull statistics.

2 | EXPERIMENTAL

2.1 | Materials of study and samples

Three different samples were fabricated using the tape casting technique: (i) monolithic samples with equiaxed microstructure (EA) containing alumina and 5 vol% tetragonal zirconia, (ii) monolithic textured alumina (TA) consisting of elongated alumina grains aligned in casting direction, and (iii) a multilayer architecture with alternating EA and TA layers designed with tailored in-plane residual stresses.

The main powder used for fabrication of monolithic as well as multilayer composites was high-purity α-Al$_2$O$_3$ (AKP-50, Sumitomo Chemicals, Tokyo, Japan) with particle size distribution from 0.09 to 0.34 μm and a mean particle size of $d_{50} = 0.20$ μm. To prevent abnormal grain growth in EA, 5 vol% of 3 mol% yttria-stabilized zirconia with a mean particle size of $d_{50} = 0.04$ μm was added to the alumina powder. In the case of TA, 5 vol% single crystal
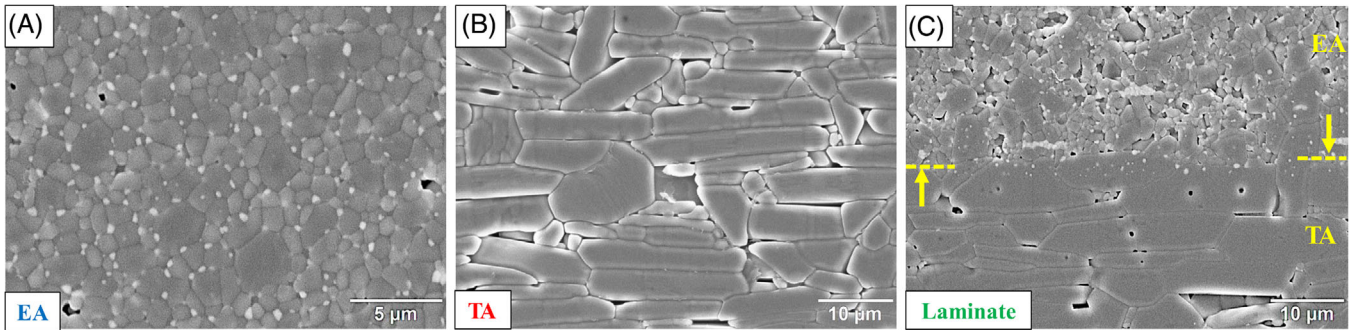
FIGURE 1 Microstructure of (A) monolithic equiaxed microstructure (EA), (B) monolithic textured alumina (TA), and (C) multilayer composite samples. The strong EA/TA interface of the laminate is indicated by yellow arrows

alumina platelets (Rona Flair® White Sapphire, EMD Performance Materials Corp., Darmstadt, Germany) with a diameter of 5–16 μm and a thickness of ~0.1 μm were used as templates together with a 0.25 wt% dopant concentration in respect to the alumina powder (CaO:SiO$_2$ = 1:1) for enhancing the templated grain growth (TGG).[31] All slurries contained an acrylic binder system. After slurry preparation and tape casting process, the specific tapes (EA and TA) were cut and stacked according to the desired design. Subsequently, uniaxial pressing (8 MPa), isostatic lamination (20 MPa), binder burn out (450°C), and cold isostatic pressing (200 MPa) of the stacked plates were performed. Afterwards, the plates were sintered at 1550°C for 4 h and the samples of study were prepared for testing. More details about slurry compositions and the processing of the layered alumina architectures can be found in previous work.[31]

To study the microstructure of the monolithic EA, TA, and the laminate, the samples were polished on the side surface up to 1 μm mirror finish using a Struers Pedemax-2 equipment (Struers Tech, DK2610 Copenhagen, Denmark) and thermally etched at 1450°C for 30 min. Subsequently, the polished side surfaces were gold coated using an Agrar Sputter coater. The images of the microstructures taken using a scanning electron microscope (JEOL JCM-6000Plus, Neoscope™, JEOL Ltd., Tokyo, Japan) can be seen in Figure 1. The microstructure of EA shows alumina grains with a size of ~2 μm and rather fine-grained zirconia (~0.5 μm) located at the triple points (see Figure 1A). Figure 1B shows the TA microstructure composing highly elongated alumina grains with length of ~20 μm and thicknesses of ~5 μm. The multilayer sample exhibits a strong EA/TA interface, as illustrated in Figure 1C.

The testing sample geometries of the prismatic bend bars prepared from the tapes were ~25 × 3 × 3 mm^3 for monolithic (EA, TA) and ~25 × 4 × 3.5 mm^3 for the layered architecture, respectively. The top surfaces were ground with D15 finish on both sides to guarantee fully flat samples for testing. Subsequently, the testing surface (one of the top surfaces) was polished up to 1 μm mirror finish using a Struers Pedemax-2 equipment.

The layered ceramic architecture consisted of two TA layers embedded within three EA alumina–zirconia layers following the sequence EA/TA/EA/TA/EA. After grinding and polishing of the outer-most EA layers, the final thickness of the individual layers was ~110 μm/300 μm/2520 μm/300 μm/110 μm, which corresponds to a volume ratio between the materials of $V_{EA}/V_{TA} \sim 5$.

The analytical estimation of the in-plane residual stresses within the alternating layers of the multilayer architecture can be obtained through the following equation[32]:

$$\sigma_{\text{res}, n} = \frac{E_n}{1 - \nu_n} (\bar{\alpha} - \alpha_n)\Delta T \qquad (1)$$

where ν_n is the Poisson's ratio (~0.22 for EA and TA), E_n is the Young's modulus (~380 GPa for both EA and TA[31]), α_n is the coefficient of thermal expansion (8.2 × 10^{-6} and 7.8 × 10^{-6} K^{-1} for EA and TA, respectively[31]) of the nth layer of each contributing material. The temperature difference is $\Delta T = T_0 - T_{\text{ref}}$, where T_0 is the room temperature and T_{ref} is the reference temperature, above which the material is assumed to be free of residual stresses (so-called stress-free temperature). In our work, T_{ref} is taken as ~1500°C, as estimated for alumina/zirconia ceramics elsewhere.[33] The average coefficient of thermal expansion for the layered system was calculated according to the following equation[32]:

$$\bar{\alpha} = \sum_{n=1}^{N} \frac{E_n t_n \alpha_n}{1 - \nu_n} \Bigg/ \sum_{n=1}^{N} \frac{E_n t_n}{1 - \nu_n} \qquad (2)$$

where t_n is the corresponding n^{th} layer thickness of the multilayer composite.

In the multilayer architecture of study, the in-plane residual stresses in the EA and TA layers resulted in ~ +50 and ~ −240 MPa, respectively.
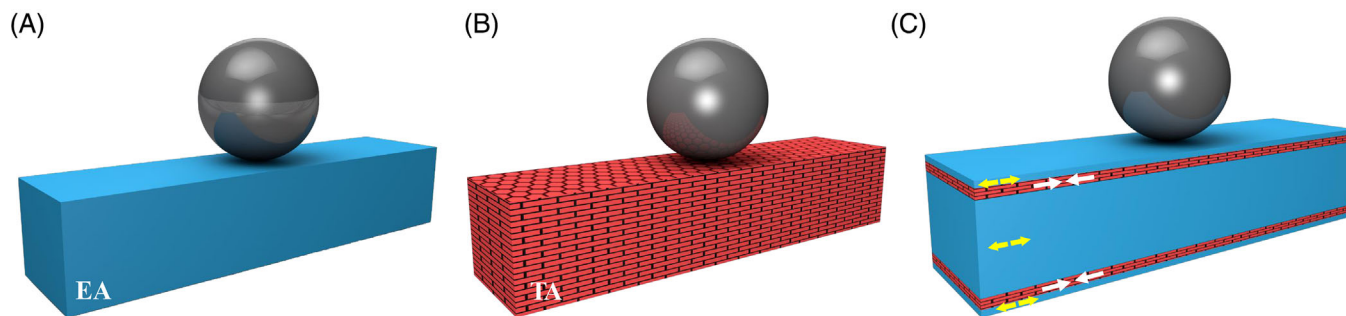
FIGURE 2 Schematic of the contact testing setup for the three samples: (A) equiaxed microstructure (EA), (B) textured alumina (TA), and (C) multilayer. In the TA-specimens, the top surface under contact loading was set parallel to the basal planes of the textured microstructure (the textured grains are illustrated as "bricks"). In the multilayer architecture, the in-plane tensile and compressive residual stresses in the EA and TA-regions are indicated by yellow and white arrows, respectively

2.2 | Testing procedure

Hertzian indentation tests were performed in ambient conditions (25°C and ~25% relative humidity) using a universal testing machine (MIDI 10-5/6x11, Messphysik, Fürstenfeld, Austria) with a load cell of 25 kN. A tungsten–carbide sphere (94WC–6Co, Kugel Pompel®, Austria) with a diameter of 4 mm was used as indenter. The EA, TA, and multilayer prismatic bar-shaped samples are schematically represented in Figure 2. We caution the reader that the contact region between sphere and specimen is approximately 10 times smaller than the width of the bar, and thus no influence of free edges on the contact stress distribution may be expected.

To detect acoustic events during the indentation cycle, AE sensors (VS150-M, Vallen Systeme GmbH, Germany) were attached onto the indenter as well as on the sample holder. This AE system allowed the accurate determination of the critical forces responsible for the initiation event corresponding to the first crack. A threshold amplitude limit of 21.9 dB was found to be sufficient to eliminate background noise. All the contact tests were carried out using a pre-load of 10 N, a displacement rate of 0.01 mm/min, and a dwell time of 10 s at the maximum load of the cycle. At least 20 spherical indentations per sample were performed to detect the crack initiation force. Depending on the type of tests, this maximum load was either deliberately selected as specific force (800, 1000, 1500, and 2000 N) for studying the crack propagation or limited by the crack initiation force as detected by the AE system to investigate the onset of cracking. In the latter case, the loading cycle was interrupted by the main unit of the AE system right after detecting the first crack initiation event. To avoid crack interactions, a distance of 2 mm between imprints within a sample was set by using a precision cross-head table. All the imprints were performed on the top surface of the stacked samples (see Figure 2).

2.3 | Damage observation

In order to study the surface damage, liquid dye penetrant (Diffu-Therm® red penetrant) was applied on all the tested sample surfaces for 24 h. The surface cracks were observed with an optical microscope (Nikon ECLIPSE LV100ND, Japan) under polarizing and non-polarizing mode. In particular, the polarizing light microscopy technique was exploited in this study for visualizing surface ring cracks at first formation stage, which otherwise would remain invisible in non-polarizing mode. To measure the depth profile of the indents as well as to visualize the corresponding surface depression in 3D, a laser scanning confocal microscope (Keyence VK-X1000, Belgium) was employed.

In the case of subsurface damage investigations, the samples were cross-sectioned by grinding and polishing starting from a side surface to the region of interest (mid-plane of the indent). Subsurface damage was observed using the optical microscope with and without polarized light. Furthermore, to study the damage patterns in detail, while avoiding possible mechanically induced damage of the zones due to polishing, ion-slicing technique (Hitachi ArBlade 5000) was employed and observations were conducted using scanning electron microscopy (Tescan Clara).

2.4 | Evaluation of data

The critical forces for crack initiation as well as their corresponding maximum tensile stresses (first principal radial stress) were analyzed according to contact Hertzian theory, as follows[34]:

$$\sigma_{\max} = (1 - 2\nu) \frac{P}{2\pi a^2} \tag{3}$$

where ν is the Poisson's ratio of the sample ($\sim$0.22 for alumina), P is the indentation load (measured crack initiation load), and a is the corresponding contact radius. This contact radius a is defined as[34]:

$$a = \left(\frac{3PR}{4E^*} \right)^{1/3} \tag{4}$$

where R is the radius of the indenter sphere, and E^* is the combined elastic modulus, which is given as follows[34]:

$$\frac{1}{E^*} = \frac{1-\nu^2}{E} + \frac{1-\nu_i^2}{E_i} \tag{5}$$

In this relation, ν_i is the Poisson's ratio of the indenter (assumed to be 0.21), E and E_i are the Young's moduli of the sample ($\sim$380 GPa[31]) and the indenter ($\sim$650 GPa[35]), respectively.

The crack initiation forces and the corresponding crack initiation stresses were analyzed in the framework of Weibull statistics.[36,37] According to Equations (3) and (4), the maximum tensile stresses, σ_{max}, are in correlation with the indentation load, P, as $\sigma_{max} \propto P^{1/3}$.

3 | RESULTS AND DISCUSSION

3.1 | Identification of damage mechanisms

Figure 3 shows a Hertzian ring crack formed on the monolithic EA system. Under an optical microscope with non-polarized mode the ring crack cannot be visualized (see Figure 3A). However, using polarized light the formation of ring cracks can be clearly verified (see Figure 3B). It may be hypothesized that at low ring crack initiation forces (RCIF) no debris on the crack after indentation occurs and

the cracks opening remains rather closed, which makes it barely observable without using special optical techniques. The typical Hertzian full-ring crack (indicated by white arrows) on the EA sample surface is associated with the first detected ring crack formation signal, after which the loading cycle was interrupted. It is worth indicating that in some cases either partial ring cracking or even simultaneous formation of ring and cone cracking were observed at the RCIF.

Figure 4 shows observed surface damages on the different ceramic architectures after Hertzian indentation tests loaded at moderate loads (up to 1000 N). Figure 4A shows surface damage on EA after indenting at a maximum load of 800 N. As can be seen, the red halo-like reflection surrounding the ring crack (Figure 4A, top) can be ascribed to the presence of cone crack as evidenced through cross-sectioning of the sample (see Figure 4A, bottom). It is thus demonstrated that damage initiation on the fine-grained polycrystalline EA material of study agrees with classical Hertzian cone cracking as has been observed in other glasses and ceramics.[20,21,38] It is worth emphasizing that this halo-like feature can only be observed due to the reflections of polarized light from the dye penetrant in shallow regions. Using the polarized light technique is a novel way to make either ring cracks visible or even to prove whether cone cracks may be formed or not, without a further need of sample cross-sectioning.

Figure 4B shows a representative surface imprint on the TA material indented up to 1000 N. Apparently, no ring crack formation can be observed, what suggests a different damage mechanism during Hertzian indentation. In this regard, the image indicates a rather crater-like pattern (surface depression) after indenting associated with a quasi-plastic deformation behavior of the textured microstructure.

Figure 4C shows a representative surface imprint on the multilayer material (with the top EA indented layer). A concurrent ring and cone cracking formation at first
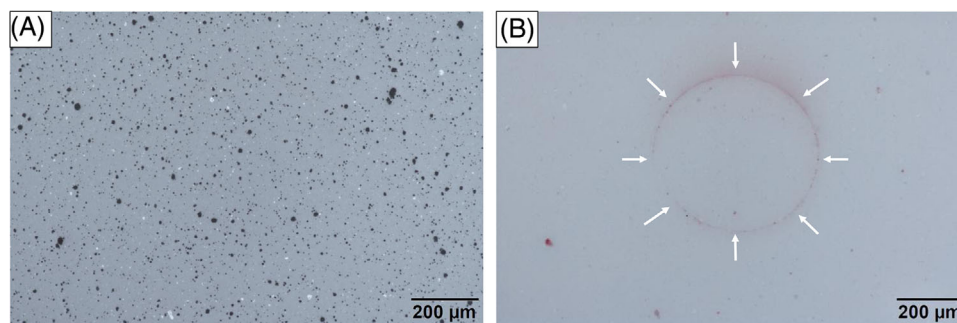

FIGURE 3 Top view of a ring crack loaded until the first acoustic emission signal (ring crack initiation force (RCIF) $\sim$850 N) was recorded on an equiaxed microstructure (EA) sample in (A) non-polarized mode, where no ring crack is visible, and (B) polarized mode, where the crack (indicated by white arrows) is detectable
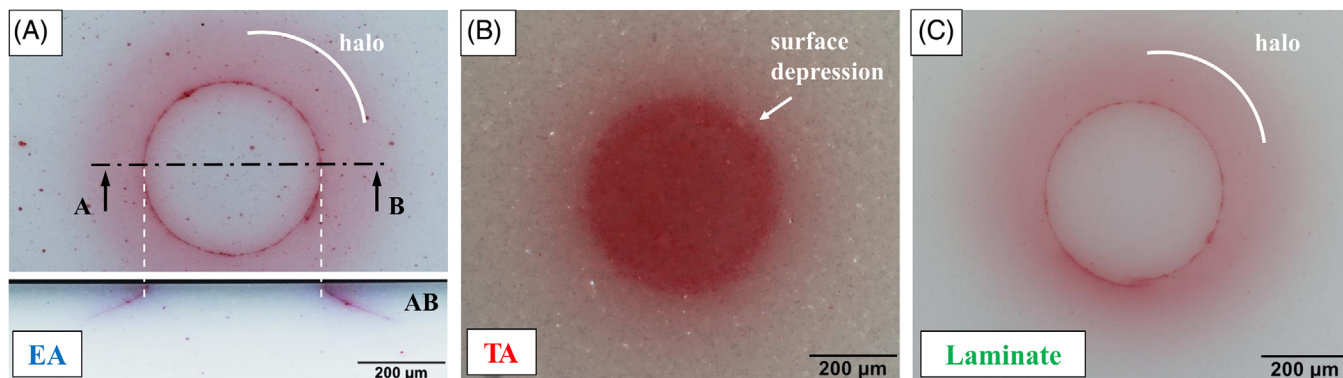
FIGURE 4 Surface damages observed on different samples at moderate loads (up to 1000 N): (A) equiaxed microstructure (EA)—formation of ring and cone crack (top) together with section view (bottom), loaded until 800 N. It is observable that the red halo-like region in top view can be associated with the cone (section view). (B) Textured alumina (TA)—showing surface depression on basal surface after loading to 1000 N. (C) Laminate—concurrent formation of ring and cone cracks (ring crack initiation forces (RCIF) ~645 N); the cone crack is indicated by the surrounded halo-like region
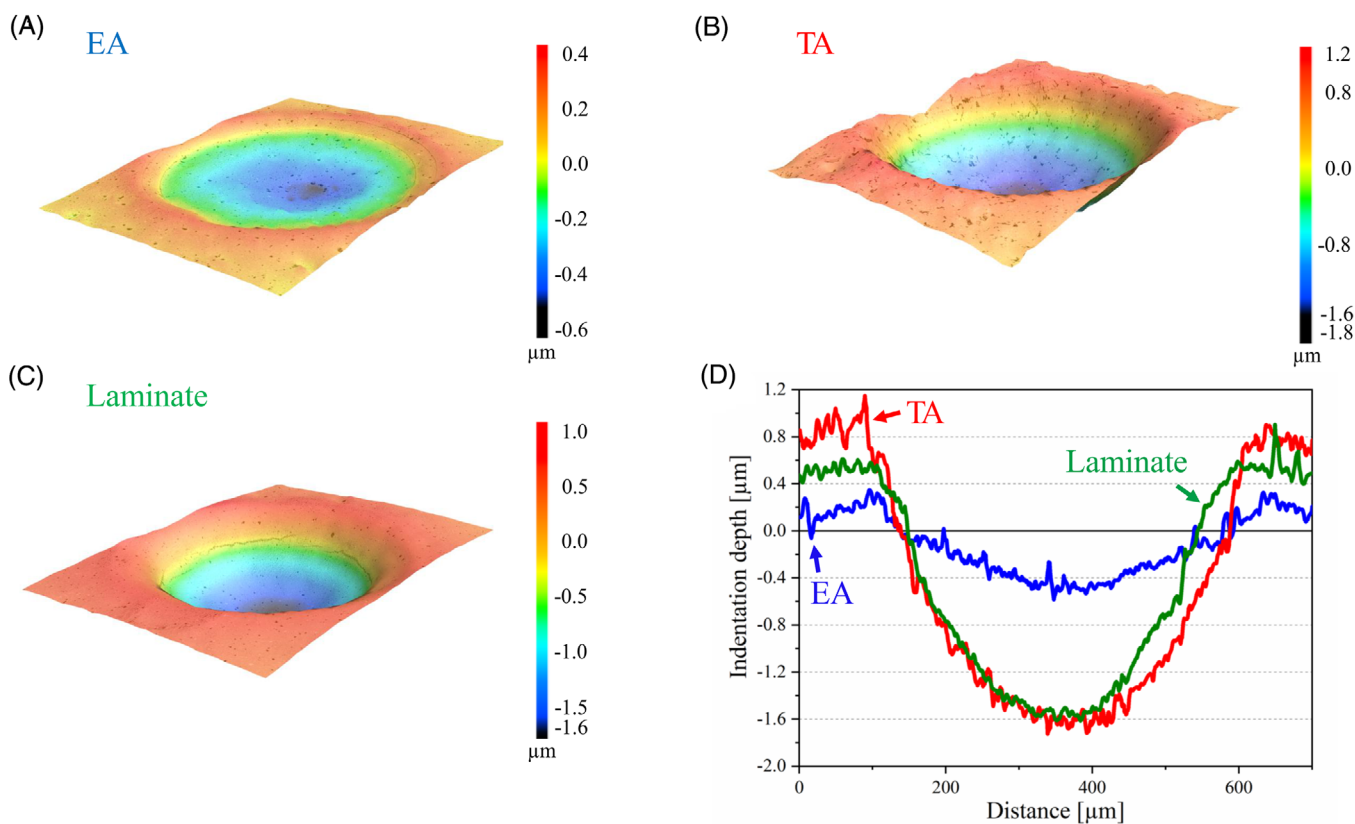

FIGURE 5 Three-dimensional reconstructions from confocal measurements of imprints performed on (A) equiaxed microstructure (EA), (B) textured alumina (TA), and (C) laminate samples. (D) Depth profiles measured at the mid-plane of the indents. The indentations were made with a maximum load of 2000 N

detected RCIF (~645 N) is revealed on the multilayer architecture. Due to the fact that the outer region of the multilayer composite is EA, the damage pattern agrees with classical ring and cone cracking as found on the monolithic EA-specimens.

For a better understanding of the imprint morphology, confocal images were taken on selected imprints at higher loads. Figure 5 shows 3D confocal images of indents made with a maximum load of 2000 N on EA, TA, and the laminate samples, together with their depth profiles.
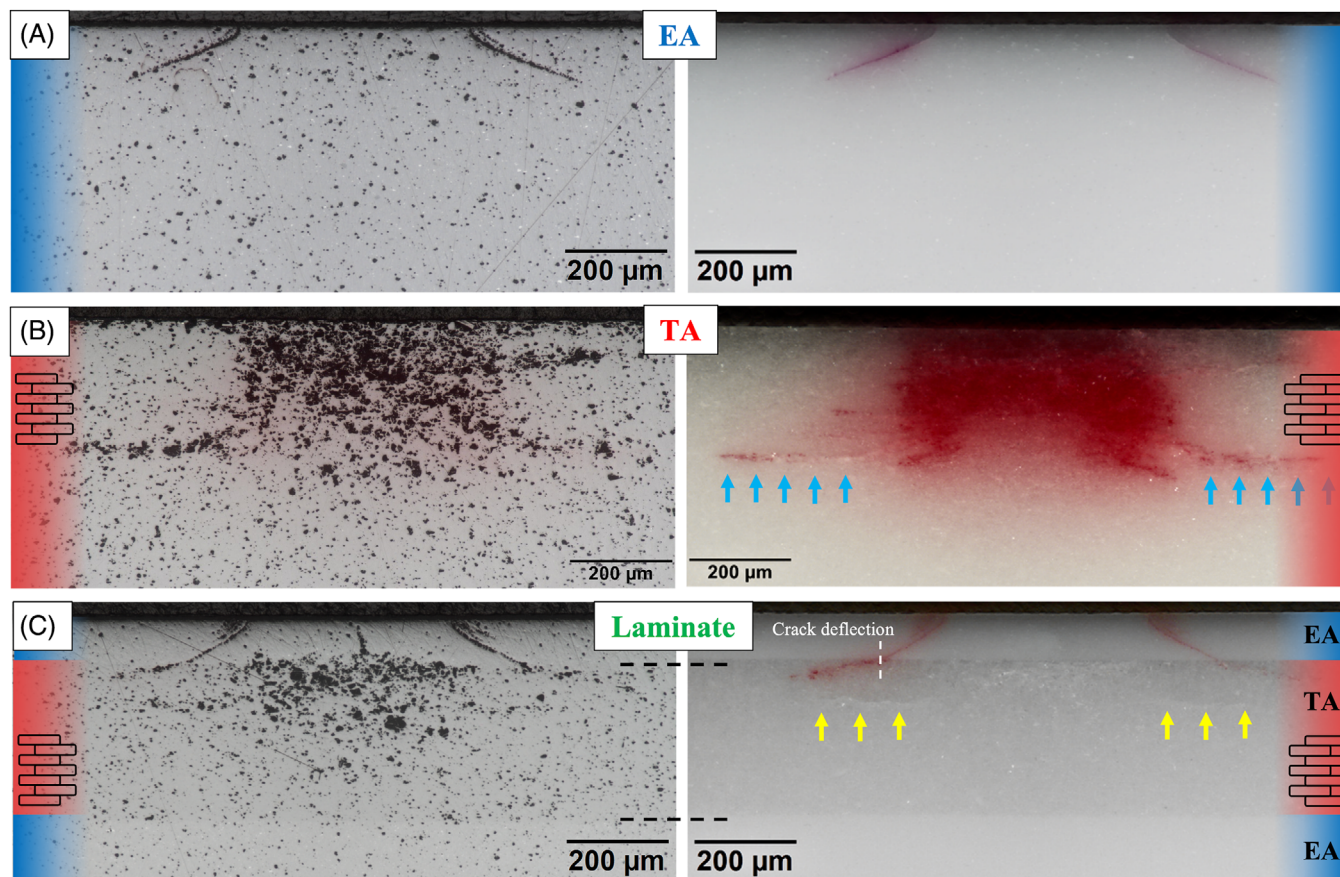
FIGURE 6 Subsurface damage zones of (A) equiaxed microstructure (EA), (B) textured alumina (TA), and (C) multilayer architecture after indenting at a maximum load of 1500 N. The left and the right sides show images taken in non-polarized and polarized mode, respectively. Arrows indicate horizontal cracks

Comparison between the confocal image of EA (Figure 5A) with those of TA (Figure 5B) and the laminate sample (Figure 5C) indicates that the textured microstructure of monolithic TA as well as the embedded TA-regions within the laminate favors surface depression by its quasi-plastic response. The depth profile (Figure 5D) reveals that in EA the surface depression is rather low with its maximum indentation depth of ∼0.6 μm of the dale. Furthermore, it can be seen that only a relatively small pile-up of about 0.4 μm occurs. In contrast to that, TA shows large pile-ups (∼0.8–1.2 μm) and a relatively high maximal indentation depth of ∼1.7 μm. Interestingly, the laminate shows similar values of pile-up (0.6–0.9 μm) and maximal depth of surface depression (∼1.6 μm), as compared to those of TA. Embedding of TA layers in the laminates may lead to the hypothesis of combined damage zones making the mechanisms more complicated to describe (combined classical Hertzian ring and cone cracking together with subsurface shearing) by only showing surface damages. Therefore, cross-sectioning was used to reveal the subsurface damage zones of the monolithic as well as multilayer samples.

Figure 6 reveals typical subsurface damage zones of EA, TA, and the multilayer after indentation with a maximum load of 1500 N, recorded in non-polarized (left) and polarized mode (right). Figure 6A shows a well-developed cone crack found on the cross-section of the EA sample. Since the applied load of 1500 N is approximately 70% higher than the measured RCIF (∼875 N for this indent), the extending cone crack shows a final depth of ∼110 μm. In contrast to that, the cross-section view of TA shows no evidence of deleterious cone cracks (see Figure 6B); however, a quasi-plastic damage zone is clearly visible. Especially, the cone cracks are best observable using polarized light microscopy, whereas the quasi-plastic deformation zones can be visualized using non-polarized light. Research done on the nature of quasi-plastic damage has reported the presence of distributed shear-fault cracks at the interface boundaries of heterogeneous alumina/calcium–hexaluminate[27,28] or at the weak interface between mica-platelets and glass matrix.[25] Furthermore, the quasi-plastic damage modes can be controlled by using coarser microstructures[22,23] or higher amount of porosities[24] and by adding specific fillers, that is, graphene platelets to
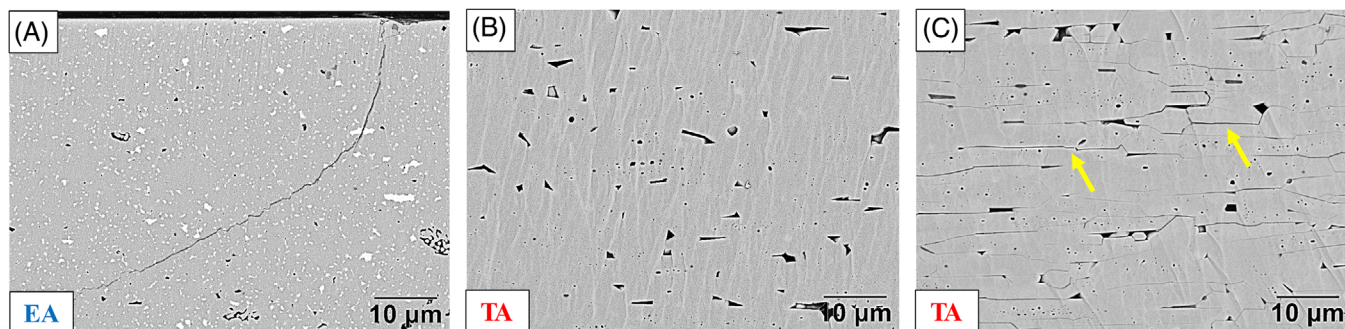
FIGURE 7 Ion-sliced images of (A) cone crack in equiaxed microstructure (EA) (load of 1500 N), (B) damage-free zone in textured alumina (TA) (unloaded), and (C) quasi-plastic damage zone in TA (1500 N)

silicon carbide as in the study of Belmonte et al.[26] In our work, the subsurface quasi-plastic damage zones within TA are a result of shear-faulting driven micro-failures at the weak basal interfaces of the textured microstructures. However, the cross-sectioning by using a polishing procedure leads to grain pull-outs and the subsurface damage zones are hardly observable. Most of the literature works mentioned above take advantage of the "bonded-interface" observations to reveal the origin of subsurface damage zones.[19,22–24,27] In our work, a novel approach was attempted exposing ion-sliced regions aiming to explain the origin of quasi-plasticity within TA samples. As comparison, the ion-sliced image of the cone crack in the EA sample is shown in Figure 7A. Figure 7B shows an ion-sliced region of TA without the subsurface deformation zone (reference position). It can be seen that this region is free from micro-failures, showing only the natural porosity of TA. In contrast to that, Figure 7C reveals the region where the maximum shear-sliding mechanisms take place. Micro-cracks extended along the weak basal planes of the textured grains (indicated by yellow arrows) are evident, consistent with the nature of quasi-plasticity prominent in the TA sample. The center of the quasi-plastic region (depth of ~100 μm) is in agreement with the zone where the highest maximum shear stress occurs ($\sim 0.5 \times a$).[19] Furthermore, a horizontal crack emanating from the elastic/plastic interface, induced during unloading, along the basal planes is visible (blue arrows in Figure 6B).

As can be seen in Figure 6C, both damage mechanisms, classical cone cracking in the outer EA-region and quasi-plastic deformation within the embedded TA layer are conspicuous in the multilayer sample. The quasi-plastic deformation zone in the TA layer is similar to that of the monolithic TA sample (see Figure 6B), indicating the same damage mechanism of intergranular micro-failures. Furthermore, a notable deflection of the cone crack path at the interface EA/TA is paramount to mention, as shown in the work of Chlup et al.,[39] where they studied the deflec-

tion of Vickers indentation cracks on dissimilar alumina–zirconia laminates. The crack deflection angles (measured in respect to the horizontal sample edge) at the interfaces of our multilayer systems were measured as <15°. Beside the crack deflection due to the dissimilar materials in the multilayer sample, further contribution from microstructural deflections along the weak basal planes of the TA grains is predominant. These effects cause the cone crack to deviate from maximum tensile stress trajectories induced during spherical indentation and thus limiting its maximal depth (~120 μm for this case). Again, horizontal cracks in the TA-region of the multilayer can be seen (indicated with yellow arrows in Figure 6C).

In order to study the propagation of cone cracks in the multilayer architecture, higher loads (2000 N) were applied in selected samples. Figure 8 shows the subsurface damage in the laminate, compared to the EA sample. Both images were taken in polarizing light mode in order to reveal the final crack depth after indenting. The final depth of the cone crack in EA loaded at 2000 N is ~200 μm (Figure 8A), which is ~90 μm longer than the cone at 1500 N, indicating stable crack growth during loading.

As can be seen in Figure 8B, the quasi-plastic damage zone is expanded and the above-mentioned horizontal cracks within the TA-region are more extended (indicated by blue arrows). However, the final depth of the cone crack was measured again ~120 μm, indicating that the cone crack is not growing with increasing load which concurs with the explanation of cone crack deviation from the trajectory of maximum stresses. Comparing the final cone crack length of ~200 μm within the monolithic EA with that of ~120 μm within the EA-region of the multilayer architecture demonstrates the exceptional damage tolerance of multilayer systems with tailored microstructures. In our design approach three beneficial mechanisms can be achieved, as can be confirmed by exposing ion-sliced region within the multilayer sample (Figure 9):
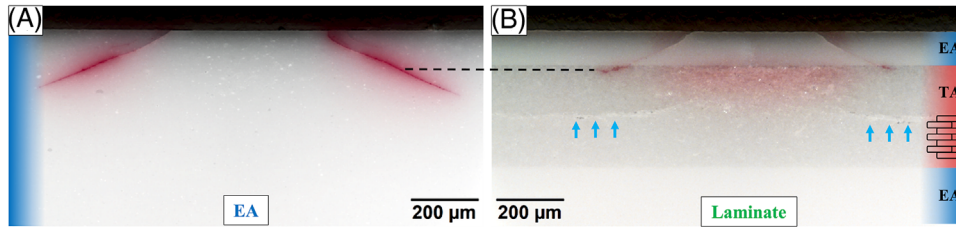
FIGURE 8 Cross-sections of (A) equiaxed microstructure (EA) and (B) the multi-material system loaded with a maximum load of 2000 N. The dashed line indicates that the maximum depth of the cone crack in the EA sample is larger than that of the multilayer sample
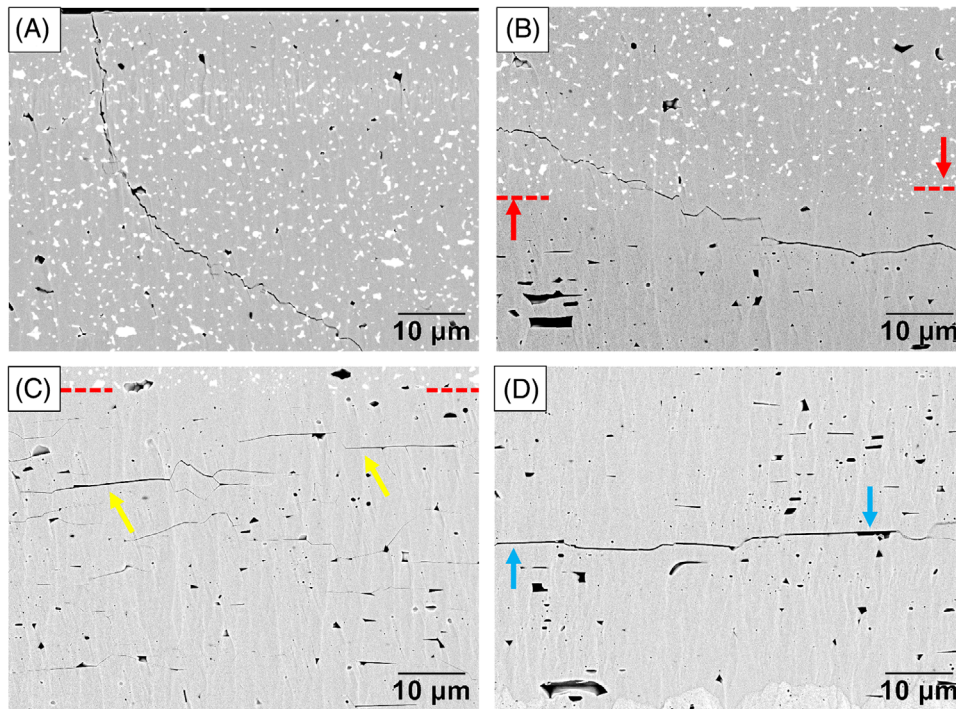

FIGURE 9 Damage patterns of the laminate exposed by ion-slicing technique (loaded with 2000 N): (A) cone crack in the equiaxed microstructure (EA)-region, (B) deflection of the cone crack at the EA/textured alumina (TA) interface (interface is indicated by red arrows), (C) quasi-plastic damage zone (micro-cracks are designated by yellow arrows), and (D) horizontal crack (indicated by blue arrows) in the TA-region of the multi-material system

(i) absorbing contact damage-induced energy within the internal TA layer by micro-crack formation (Figure 9C), (ii) deflection of the cone crack at the EA/TA interfaces, and (iii) microstructural crack deflection at the weak basal interfaces of the aligned textured grains, which favors the rather horizontally crack propagation in a step-like fashion through the embedded TA-region, as can be seen in Figure 9B. The above-mentioned horizontal crack within the TA-region is revealed in Figure 9D. For the sake of comparison, the cone crack in the EA-region of the laminate, similar to that in monolithic EA, is shown in Figure 9A. The combination of these mechanisms may alleviate deleterious effects associated with cone cracking by limiting its final crack depth regardless of the indenting load.

TABLE 1 Measured ring crack radius (a_c) as well as the calculated contact radius (a) for the equiaxed microstructure (EA) and the laminate, respectively

Sample	Ring crack radius, a_c (μm)	Contact radius, a (μm)
EA	212 ± 16	164 ± 6
Laminate	206 ± 17	159 ± 7

3.2 | Assessment of damage

The measured ring crack radius, a_c, as well as the calculated contact radius a (evaluated according to Equation (4)), of the EA and the laminate system can be found in Table 1, respectively.

It can be seen that the ring crack radius, a_c, is for both systems approximately 30% higher than the calculated contact radius, a, yielding to the observation that ring crack initiation takes place outside of the contact circumference. The ratio a_c/a with the value of ~1.3 is in good agreement with the reported ones found in literature for different indented ceramics and glasses.[20,21,40,41]

To study the influence of the tensile residual stresses in the EA-region of the multilayer on the cone crack angle, the angle (with respect to horizontal sample edge) was measured as ~27.2 ± 2.5° and 21.6 ± 0.5° on selected samples of the multilayer and the EA-monolith, respectively. This finding shows that tensile residual stresses of ~50 MPa in the surface EA-regions increase the cone crack angle by ~6°, which is consistent with the numerical predictions of Ceseracciu et al.[42]

Figure 10 represents diagrams, where the energy of acoustic events is plotted versus the corresponding load during indentation, for one representative indent of EA, TA, and the multilayer samples, respectively, measured under Hertzian indentation over a complete loading cycle. The energy is expressed in energy units (eu), where 1 eu corresponds to 10^{-14} V^2 s.[43] As can be seen in Figure 10A, relatively high energies are emitted (>1000 eu) as long as classical Hertzian ring and/or cone cracking occurs during loading. For this representative measurement, it was found that the first acoustic event ($E \sim 1620$ eu) occurring at the RCIF (~875 N), was responsible for the formation of ring cracks. After the ring cracking event, even higher energy was measured (~53 400 eu) at a load of approximately 1330 N. The second AE event corresponds to the pop-in of the cone crack. It is hypothesized that the third signal ($E \sim 1735$ eu) can be associated with stable crack growth of the cone crack at higher loads. However, the reader is cautioned that in EA, ring and cone cracking are not always considered to occur separately, but may also take place simultaneously as discussed in Section 3.1.

In contrast to that, Figure 10B shows a high number of low-energy signals (<100 eu) starting at lower loads. The first signal at 260 N with an energy of ~1 eu could not be associated with surface damage. As the load is increased during the indentation cycle, low-energy signals are emitted in a frequent fashion. These low-energy patterns may indicate the formation of micro-cracks during subsurface shear faulting. The first higher peak of the low-energy signals ($E \sim 70$ eu) at the load of 570 N can be correlated with the start of a detectable surface impression on the surface of TA. To our best knowledge, this is the first report, showing the evidence of distinguishing the mechanisms of damage (classical ring/cone cracking or quasi-plastic deformation) by interpreting the AE signals. Figure 10C reveals the detected energy signals versus load of the multilayer sample. Initially, low-energy signals (<10 eu) occur in a frequent manner comparable to the signals detected in TA
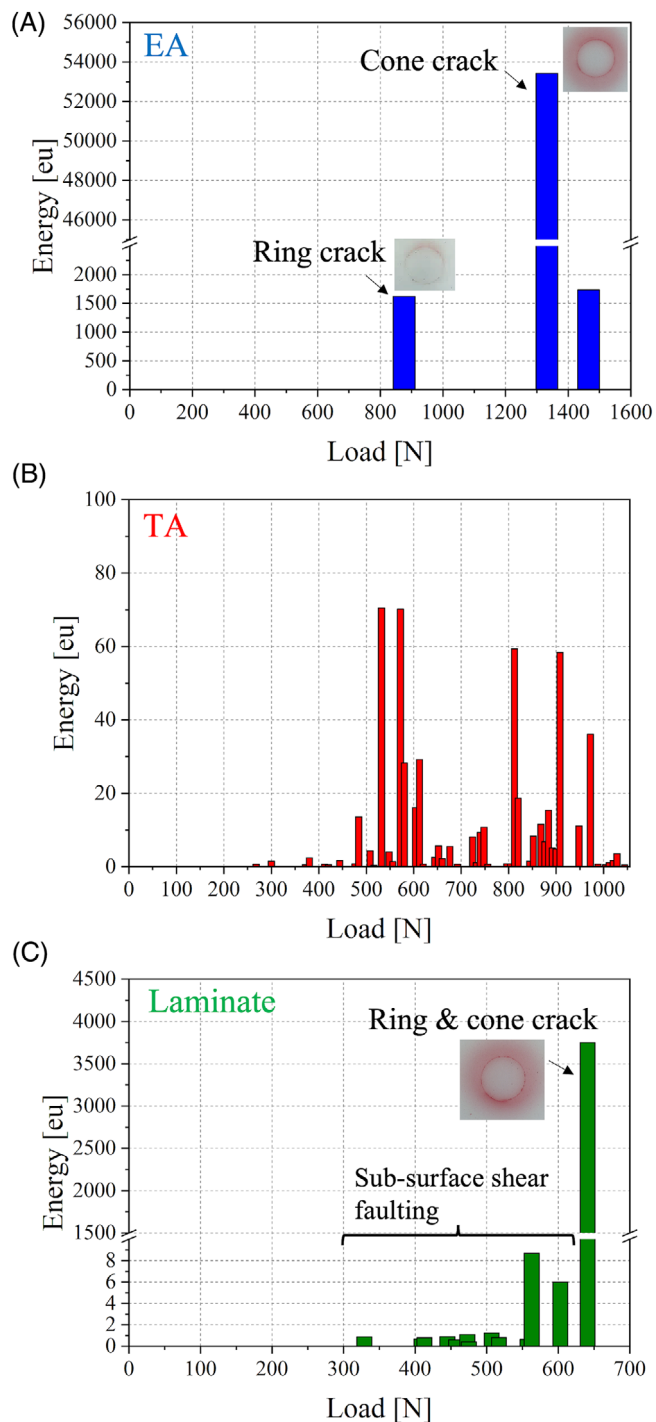

FIGURE 10 Diagrams of the acoustic emission energies plotted versus the load from indentations made on (A) equiaxed microstructure (EA), (B) textured alumina (TA), and (C) laminate

(see Figure 10B). The first detectable surface damage (ring and cone crack) was found at the load of approximately 650 N at the corresponding high-energy peak of ~3750 eu. As already discussed in Section 3.1, both damage zones are prominent in the multilayer sample after Hertzian contact testing; classical ring and cone cracks in the EA outer region and quasi-plastic subsurface damage in the
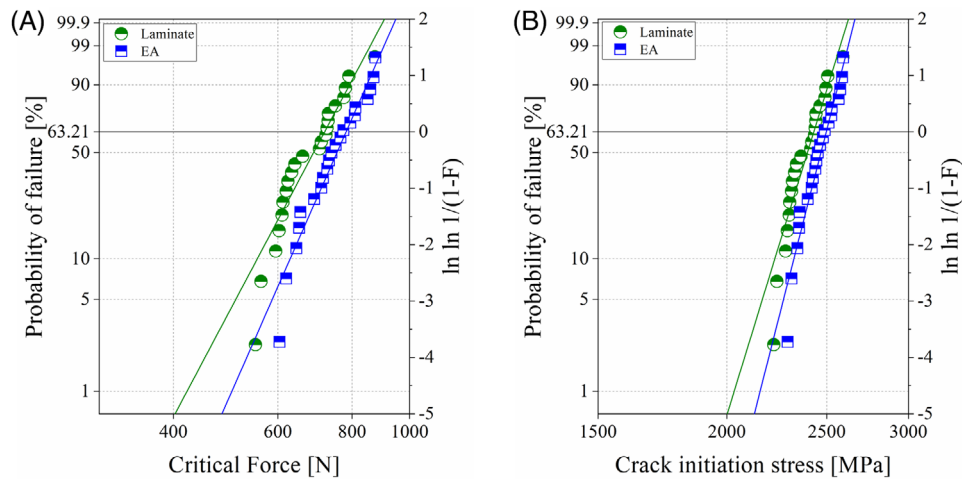
FIGURE 11 (A) Ring crack initiation forces (RCIF) and (B) calculated RCIS distributions of equiaxed microstructure (EA) and the multilayer architecture. The lines represent the best fit according to the maximum-likelihood method

embedded TA-regions. Due to the fact that the emitted signals at loads lower than ∼600 N are similar to the energy values of TA, subsurface micro-cracking can be associated within this loading range. At higher loads, high-energy peaks of the laminate are found to be in the order of magnitude of energies detected in EA and are evident for being considered as RCIF. These findings show that subsurface damage mechanisms within the embedded TA layer is prior to classical ring crack initiation, as long as the maximum shear stress responsible for subsurface shear faulting lies within the TA layer and not in the EA layer. In the light of these results, it can be concluded that the response of the layered alumina architecture to contact loading may be controlled by designing the thickness of the outermost layer with respect to the depth of the shear stress field. This will be investigated in future work.

3.3 | Evaluation of crack initiation stress

In order to discuss the influence of residual stresses on the data distributions, statistical analysis of the measured data was carried out. Figure 11A shows the RCIF distributions of the monolithic EA as well as the laminate system. In this Weibull diagram, the probability of failure is plotted versus the critical forces for ring crack initiation. In Figure 11B, the corresponding ring crack initiation stress (RCIS) distributions are represented for both systems (EA and laminate). The probability of failure is plotted against the maximum tensile stresses as calculated according to Equation (3). The characteristic RCIF as well as the characteristic RCIS can be interpreted as the critical force or stress where the probability of failure is ∼63%. The Weibull modulus of the corresponding RCIF as well as RCIS data is a measure for the scatter and describes the width of the distributions.

TABLE 2 Characteristic ring crack initiation force (RCIF) (F_0), characteristic ring crack initiation stress (RCIS) (σ_0), Weibull modulus (m), and the corresponding 90% confidence intervals of monolithic equiaxed microstructure (EA) and the laminate

Sample	Characteristic RCIF, F_0 (N) and Weibull modulus, m	Characteristic RCIS, σ_0 (MPa) and Weibull modulus, m
EA	$F_0 = 782$ [751–814] $m = 10$ [7–13]	$\sigma_0 = 2497$ [2464–2531] $m = 31$ [22–39]
Laminate	$F_0 = 719$ [686–754] $m = 9$ [6–11]	$\sigma_0 = 2428$ [2391–2467] $m = 26$ [18–32]

In both diagrams, the lines represent the best fits of the corresponding data sets according to the maximum-likelihood method. All the Weibull parameters are listed in Table 2.

The characteristic RCIF of EA is about 60 N higher than that of the laminate with comparable Weibull modulus. In the case of the RCIS distributions, it can be noticed that the characteristic RCIS of EA is ∼70 MPa higher than that of the laminate, with the difference corresponding to the tensile residual stresses. The difference of ∼70 MPa is well comparable with the estimated residual stresses according to Equation (1) (∼50 MPa). These results indicate the high accuracy of the methodology employed and suggests the possibility of using spherical contact indentation techniques to estimate the residual stress state of ceramic-based components.

4 | CONCLUSIONS

The contact damage behavior under spherical indentation of layered alumina architectures designed with embedded textured layers under in-plane compressive

residual stresses was investigated. It is found that the quasi-plastic deformation associated with micro-cracking along basal planes within the embedded textured layer upon loading, enhances the capacity for damage absorption, compared to the reference bulk material with equiaxed microstructure. For higher applied loads, the cone cracks that extend from the surface ring crack can be deflected at the textured layer and guided parallel to the layer plane, thus preventing the multilayer architecture from catastrophic failure. The positive combined effect of textured architecture and compressive residual stress in subsurface layers shows the potential for the design of ceramic components with enhanced contact damage tolerance.

ORCID
Abdullah Jabr https://orcid.org/0000-0002-0695-6906
Raul Bermejo https://orcid.org/0000-0002-6891-3653

REFERENCES
1. Munz D, Fett T. Ceramics: mechanical properties, failure behaviour, materials selection. 2nd ed. Berlin: Springer; 2001.
2. Carter CB, Norton MG. Ceramic materials: science and engineering. New York: Springer; 2013.
3. Danzer R, Lube T, Supancic P, Damani R. Fracture of ceramics. Adv Eng Mater. 2008;10:275–98.
4. Morrell R. Fractography of brittle materials: measurement good practice guide no. 15. Teddington, UK: National Physical Laboratory; 1999.
5. Lange FF. Powder processing science and technology for increased reliability. J Am Ceram Soc. 1989;72:3–15.
6. Lawn BR. Fracture of brittle solids. Cambridge: Cambridge University Press; 1993.
7. Rao M, Sanchez-Herencia J, Beltz G, McMeeking RM, Lange F. Laminar ceramics that exhibit a threshold strength. Science 1999;286:102–5.
8. Bermejo R, Torres Y, Baudín C, Sánchez-Herencia AJ, Pascual J, Anglada M, et al. Threshold strength evaluation on an Al_2O_3–ZrO_2 multilayered system. J Eur Ceram Soc. 2007;27:1443–8.
9. Bermejo R, Torres Y, Sánchez-Herencia AJ, Baudín C, Anglada M, Llanes L, et al. Residual stresses, strength and toughness of laminates with different layer thickness ratios. Acta Mater. 2006;54:4745–57.
10. Sglavo VM, Paternoster M, Bertoldi M. Tailored residual stresses in high reliability alumina-mullite ceramic laminates. J Am Ceram Soc. 2005;88:2826–32.
11. Costabile A, Sglavo VM. Influence of the architecture on the mechanical performances of alumina-zirconia-mullite ceramic laminates. Adv Sci Technol. 2006;45:1103–8.
12. Sglavo VM, de Genua F, Molinari A, Casari F. Alumina/silicon carbide laminated composites by spark plasma sintering. J Am Ceram Soc. 2009;92:2693–7.
13. Wegst UGK, Bai H, Saiz E, Tomsia AP, Ritchie RO. Bioinspired structural materials. Nat Mater. 2015;14:23–36.
14. Pavlacka RJ, Messing GL. Processing and mechanical response of highly textured Al_2O_3. J Eur Ceram Soc. 2010;30:2917–25.
15. Chang Y, Bermejo R, Messing GL. Improved fracture behavior of alumina microstructural composites with highly textured compressive layers. J Am Ceram Soc. 2014;97:3643–51.
16. Bermejo R. "Toward seashells under stress": bioinspired concepts to design tough layered ceramic composites. J Eur Ceram Soc. 2017;37:3823–39.
17. Hertz H. Ueber die Berührung fester elastischer Körper. J Reine Angew Math. 1882;92:156–71.
18. Lawn BR, Wiederhorn SM, Johnson HH. Strength degradation of brittle surfaces: blunt indenters. J Am Ceram Soc. 1975;58:428–32.
19. Lawn BR. Indentation of ceramics with spheres: a century after Hertz. J Am Ceram Soc. 1998;81:1977–94.
20. Tillett JPA. Fracture of glass by spherical indenters. Proc Phys Soc B. 1956;69:47–54.
21. Wereszczak AA, Johanns KE, Jadaan OM. Hertzian ring crack initiation in hot-pressed silicon carbides. J Am Ceram Soc. 2009;92:1788–95.
22. Lee SK, Wuttiphan S, Lawn BR. Role of microstructure in Hertzian contact damage in silicon nitride: I, mechanical characterization. J Am Ceram Soc. 1997;80:2367–81.
23. Guiberteau F, Padture NP, Lawn BR. Effect of grain size on Hertzian contact damage in alumina. J Am Ceram Soc. 1994;77:1825–31.
24. Latella BA, OConnor BH, Padture NP, Lawn BR. Hertzian contact damage in porous alumina ceramics. J Am Ceram Soc. 1997;80:1027–31.
25. Cai H, Kalceff SMA, Lawn BR. Deformation and fracture of mica-containing glass-ceramics in Hertzian contacts. J Mater Res. 1994;9:762–70.
26. Belmonte M, Miranzo P, Osendi MI. Contact damage resistant SiC/graphene nanofiller composites. J Eur Ceram Soc. 2018;38:41–5.
27. An L, Chan HM, Padture NP, Lawn BR. Damage-resistant alumina-based layer composites. J Mater Res. 1996;11:204–10.
28. Ha H-C, Chan HM, Nied HF. Hertzian contact behavior of alumina-based trilayer composites: experimental observation and FEM analysis. Acta Mater. 2001;49:2453–61.
29. Miranda P, Pajares A, Guiberteau F, Deng Y, Lawn BR. Designing damage-resistant brittle-coating structures: I. Bilayers. Acta Mater. 2003;51:4347–56.
30. Miranda P, Pajares A, Guiberteau F, Deng Y, Zhao H, Lawn BR. Designing damage-resistant brittle-coating structures: II. Trilayers. Acta Mater. 2003;51:4357–65.
31. Hofer A-K, Walton R, Ševeček O, Messing GL, Bermejo R. Design of damage tolerant and crack-free layered ceramics with textured microstructure. J Eur Ceram Soc. 2020;40:427–35.
32. Sglavo VM, Bertoldi M. Design and production of ceramic laminates with high mechanical resistance and reliability. Acta Mater. 2006;54:4929–37.

33. Chlup Z, Hadraba H, Drdlik D, Maca K, Dlouhy I, Bermejo R. On the determination of the stress-free temperature for alumina–zirconia multilayer structures. Ceram Int. 2014;40:5787–93.

34. Fischer-Cripps AC. Introduction to contact mechanics. Boston, MA: Springer Science + Business Media LLC; 2007.

35. Santhanam AT. Application of transition metal carbides and nitrides in industrial tools. In: Oyama ST, editor. The chemistry of transition metal carbides and nitrides. Dordrecht, Netherlands: Springer; 1996. p. 28–52.

36. Weibull W. A statistical distribution function of wide applicability. J Appl Mech. 1951;18:293–7.

37. EN 843-5. Advanced technical ceramics—monolithic ceramics—mechanical properties at room temperature—Part 5: statistical analysis. 1996.

38. Wade J, Ghosh S, Claydon P, Wu H. Contact damage of silicon carbide ceramics with different grain structures measured by Hertzian and Vickers indentation. J Eur Ceram Soc. 2015;35:1725–36.

39. Chlup Z, Novotná L, Šiška F, Drdlík D, Hadraba H. Effect of residual stresses to the crack path in alumina/zirconia laminates. J Eur Ceram Soc. 2020;40:5810–8.

40. Marimuthu KP, Rickhey F, Lee JH, Lee H. Spherical indentation for brittle fracture toughness evaluation by considering kinked-cone-crack. J Eur Ceram Soc. 2017;37:381–91.

41. Turner DN, Smith PD, Rotsey WB. Hertzian stress cracks in beryllia and glass. J Am Ceram Soc. 1967;50:594–8.

42. Ceseracciu L, Anglada M, Jiménez-Piqué E. Hertzian cone crack propagation on polycrystalline materials: role of R-curve and residual stresses. Acta Mater. 2008;56:265–73.

43. Vallen Systeme GmbH. Acoustic emission system AMSY-5 system description. Available from: https://www.vallen.de/zdownload/pdf/y5sd0911.pdf. Accessed 1 October 2021.